



# Numerical investigation of the maneuverability of ships advancing in the non-uniform flow and shallow water areas

Xiaoya Tang<sup>a,b,c</sup>, Sichen Tong<sup>a,b,\*</sup>, Guoxian Huang<sup>c,d</sup>, Guangxiang Xu<sup>a,b</sup>

<sup>a</sup> School of River and Ocean Engineering, Chongqing JiaoTong University, 66 Xuefu Rd., Chongqing, 400074, China

<sup>b</sup> National Engineering Research Center for Inland Waterway Regulation, 66 Xuefu Rd., Chongqing, 400074, China

<sup>c</sup> Chinese Research Academy of Environmental Sciences, 8 Dayangfang., Beijing, 100012, China

<sup>d</sup> State Key Laboratory of Plateau Ecology and Agriculture, Qinghai University, Xining, 810016, China

## ARTICLE INFO

### Keywords:

Numerical model of ship maneuvering motion

Shallow water effect

Empirical methods

Fourth-order Runge–Kutta method

## ABSTRACT

Sailing attitude would experience many changes when ship entering shallow water, due to the hydrodynamic interaction between ship hull and seabed or riverbed which can be expressed in a significant increase in resistance, sinkage and trim and can engender the safety of ships. A numerical model of ship maneuvering motion that takes account of the shallow water effect is proposed based on the Maneuvering Mathematical Modeling Group (MMG) model. Flow field data solved based on a numerical model of non – uniform flow serves as the basis for calculating hydrodynamic forces of the ship model. Simulations of straightforward, turning and zig-zag motions are performed on a cargo ship using various empirical methods and the fourth-order Runge – Kutta method. Ship trajectories for varying depth-draft ratio, rudder angle and flow velocity are compared, indicating that shallow water effect would increase ship sailing resistance and decrease maneuverability. Result shows that ship maneuverability would be reduced as the depth-draft ratio decrease when ship sailing in shallow water. Application of the model in a typical mountainous river reveals that the model can reasonably simulate the shallow water effect. The study could be a valuable reference for further investigation on shallow water effect, as well as providing guidance on ship maneuvering in shallow waterways.

## 1. Introduction

Natural rivers are basically non-uniform flow due to irregular boundaries. Traditionally the river flow was treated as uniform flow to simplify the calculations of hydrodynamic forces on ship maneuverability. However, influence of simple non-uniform flow is usually determined via a generalized method, namely making assumptions about the flow field of the reach. This method can simplify calculations and improve computational efficiency of the simulation, which is suitable for still-water areas or areas in which the flow is highly uniform. Adverse navigation flow conditions are common phenomena for inland and mountainous waterways, including flow velocity, flow direction, and water flow surface slope, etc. Uniform flow or generalized non-uniform flow methods are typically implemented. However, it is difficult to reflect the characteristics and influence of non-uniform flow on ship maneuverability in the actual river due to over-simplified flow patterns.

With the rapid development of shipping industry it is a competitive

alternative transport mode for passengers and cargo especially at much lower costs than via the other transport modes. A clear international tendency of increase in ship number can be observed due to the growing demand for ships to transport various products (Debaillon, 2010; Meng and Wan, 2016), so the risk of navigating of ships in shallow water tends to increase. In mountainous waterways the most important factor affects the navigation is the restriction of water depth. The change in water depth leads to a strong interaction between the ship and the waterway bed. Note that  $d$  is the ship draft and  $h$  is the water depth of waterway. The effects of water depth on the ship maneuverability shallow water effects on sailing ships are known to increase significantly starting at a range of depth to draft ratio between  $1.5 < h/d < 3$  (Razgallah et al., 2018). Insufficient water depth is a common occurrence and easy to engender the shallow water effect in inland waterways, and especially in mountainous rivers. Thus, difficulties and hazards associated with ship handling in mountainous waterways are increasing because of the shallow water depth (Maimun et al., 2013). When entering shallow water, a number of changes arise owing to the hydrodynamic interaction between the bottom of the ship hull and the riverbed. In general, the

\* Corresponding author. School of River and Ocean Engineering, Chongqing JiaoTong University, 66 Xuefu Rd., Chongqing, 400074, China.

E-mail address: [tongsichen@163.com](mailto:tongsichen@163.com) (S. Tong).

<https://doi.org/10.1016/j.oceaneng.2019.106679>

Received 12 October 2018; Received in revised form 29 September 2019; Accepted 2 November 2019

Available online 16 November 2019

0029-8018/© 2019 Elsevier Ltd. All rights reserved.

**List of symbols**

$o - xyz$	Ship fixed coordinate system with midship origin	$t_P$	Thrust deduction coefficient
$o_0 - x_0y_0z_0$	Spatial fixed coordinate system	$f_e$	Parameter of earth rotation
$\psi$	Heading angle	$C$	Source term
$\delta$	Rudder angle	$\nu_t$	Turbulent viscosity coefficient
$r$	Yaw rate	$T$	Propeller thrust
$\beta$	Hull drift angle at midship	$J_P$	Propeller advanced ratio
$U$	Ship resultant speed relative to the flow ( $= \sqrt{u_m^2 + v_m^2}$ )	$K_T$	Propeller thrust open water characteristic
$u_\xi$	Flow velocity in the direction of $\xi$ in body-fitted curvilinear coordinate system	$D_P$	Propeller diameter
$v_\eta$	Flow velocity in the direction of $\eta$ in body-fitted curvilinear coordinate system	$w_P$	Wake fraction at propeller position
$u_m$	Ship speed relative to the flow in the direction of $x$	$w_{P0}$	Wake fraction at propeller position in sailing ahead
$v_m$	Ship speed relative to the flow in the direction of $y$	$\beta_P$	Geometrical inflow angle to propeller in maneuvering motions
$u_x$	Ship speed relative to the river bank in the direction of $x$	$t_R$	Steering resistance deduction coefficient
$u_y$	Ship speed relative to the river bank in the direction of $y$	$F_N$	Rudder normal force
$u_{cx}$	Absolute flow velocity component in the direction of $x$	$a_H$	Rudder force increase factor
$u_{cy}$	Absolute flow velocity component in the direction of $y$	$x_R$	Longitudinal coordinate of rudder position
$m$	Ship's mass	$x_H$	Longitudinal coordinate of acting point of the additional lateral force
$F_x, F_y$	Surge force and lateral force acting on ship	$C_b$	Block coefficient
$M_Z$	Yaw moment acting on ship around center of gravity	$A_R$	Profile area of working part of mariner rudder
$I_{zG}$	Moment of inertia of ship around center of gravity	$U_R$	Resultant inflow velocity to rudder
$X, Y, N$	Surge force, lateral force, Yaw moment around midship except added mass components	$f_\alpha$	Rudder lift gradient coefficient
$J_z$	Added moment of inertia	$\alpha_R$	Effective inflow angle to rudder
$x_G$	Longitudinal coordinate of center of gravity of ship	$w_R$	Wake fraction at the rudder area where it is not hit by the propeller slip stream
$m_x, m_y$	Added mass of $x$ axis direction and $y$ axis direction, respectively	$\lambda_R$	Aspect ratio of the rudder
$X_H, Y_H, N_H$	Surge force, lateral force, yaw moment around midship acting on ship hull except added mass components $X_P$ (Surge force due to propeller)	$\lambda_e$	Effective aspect ratio of ship supposed as a wing
$X_R, Y_R, N_R$	Surge force, lateral force, yaw moment around midship by steering	$R, R_V, R_J$	Navigation resistance, flow resistance, slope resistance
$\rho$	Water density	$R_f, R_r$	Frictional resistance and residual resistance
$L$	Ship length	$f_1$	Friction coefficient
$d$	Ship draft	$A_s$	Wetted surface area
$Y'_v, N'_v$	Linear hydrodynamic derivatives with respect to lateral velocity	$L_W$	Waterline length of ship
$Y'_R, N'_R$	Linear hydrodynamic derivatives with respect to yaw moment	$B$	Ship width
$t$	Time	$V_s$	Ship sailing speed
$\gamma_R$	Flow-straightening coefficient	$V_{cp}$	Longitudinal surface mean flow velocity
$\beta_R$	Effective inflow angle to rudder in maneuvering motions	$V_a$	The minimum sailing speed of opposite bank under the influence of flow resistance and slope resistance
$Z$	Water level	$\xi_1$	Coefficient of residual resistance
$h$	Water depth	$A_m$	Area of midship section of ship wetted section
$C_{th}, C_{t\infty}$	Straightforward-moving total resistance coefficients in shallow and deep water, respectively	$\beta_c$	Coefficient of ship cross-section
		$V_F$	Absolute flow velocity of the ship's position obtained by the interpolation flow field
		$C_c$	Coefficient of cross-section of waterway
		$A_c$	Flow area of cross-section of the waterway
		$\lambda$	Aspect ratio of ship supposed as a wing
		$\Gamma$	Diffusion coefficient
		$\varphi$	Dependent variable

flow velocity between the bottom of the ship hull and the riverbed increases, which are expressed in a pronounced increase in sinkage, trim and resistance (Tezdogan et al., 2015b; Terziev et al., 2018). As the ship travels forward, it may lead to the squat sometimes resulting in undesirable grounding (Du et al., 2018).

Ship behaviors in shallow water are closely related to safe navigation, attracting much attention, a series of studies of the ship behaviors in shallow water have been carried out worldwide (Zou and Larsson, 2013; He et al., 2016). Currently, numerical methods are more prone to simulate ship behaviors in shallow water. Delefortrie and Vantorre (2007) simulated the maneuvering behavior of container carriers in shallow water, and presented the empirical expressions for the water depth dependence of mathematical models suited for the simulation of

ship maneuvers. Based on the linear slender-body assumption, Gourlay (2008) developed linear slender-body numerical methods to predict the sinkage and trim of ship sailing in shallow water. Tezdogan et al., 2015a fully adopted the nonlinear-unsteady RANS simulation to predict the squat and resistance of a model-scale Duisburg Test Case container ship. Petru (2017) conducted the CFD simulations for the purpose of observing the effects of limited water depth on sailing ship hull in two domains, one with a depth of 20.35 m and the other with a depth 6.85 m, and results implied that the effects related mainly to change in pressure, velocity, forces and torques acting on the ship hull. Besides, there are also studies on the effect of shallow water on parameters related to hull design. For instance, Rotteveel et al. (2017) investigated the effect that water depth has on the optimal choice of design parameters, such as the

athwart ship's propeller location, the tunnel top curvature, the flat-of-bottom shape in the stern region and the stern bilge radius. The effect of shallow water on sailing ahead of ships have been studied well, however, there is still room for study on maneuverability of ships in shallow waters such as mountainous rivers and canals.

Shallow water effect induces a series of adverse effects on the ship, including reduced speed as a consequence of increased resistance, reduced rudder effect, and degraded turning performance (Pacuraru and Domnisoru, 2017). According to some researchers, ships experience a drop in speed of up to 30% upon entering shallow waters (Tezdogan et al., 2015b). This value can rise up to 60% when operating in rivers or canals (Barrass, 2012). Such a dramatic speed reduction is directly attributable to the increase in resistance and the change in maneuvering characteristics. Creation of reliable mathematical models for ship maneuvering with due account for the shallow water effect is also very desirable as if such models are implemented in bridge simulators, navigators, and sailor can be better trained and prepared to complicated maneuvering phenomena (Sutulo et al., 2010). From the viewpoint of ship navigation safety, it is meaningful to simulate the maneuvering behavior of a ship in shallow water (Wei et al., 2017), which contributes to making reasonable decisions, such as the regulation of ship speed and navigation direction in the shallow water, as well as estimating the safe ship speed in advance.

In the study the numerical model of non-uniform flow is developed, and flow field calculated by the model is applied to solve the hydrodynamic forces acting on the ship. In addition, a widely used numerical model known as the maneuvering mathematical group (MMG) is proposed. The MMG model is also known as a modular model, is one of the solutions for ship maneuvering motion simulations developed in Japan (Lin-jia et al., 2013; Yasukawa and Yoshimura, 2015; Reichel, 2017). Then, a new ship maneuvering numerical model that takes account of the shallow water effect is developed as based on the deep-water model by correcting the hydrodynamic derivatives. Numerical simulations of straightforward, turning, and zig-zag motions are conducted on a cargo ship, and ship trajectories in shallow water for varying the depth-draft ratio, rudder angle and flow velocity are compared. Flow fields for two rapids of the Lancang River are simulated, aiming to providing the necessary flow field data for the maneuvering simulation of the ship in the actual river. The main objective of the research is to investigate the effect of shallow water on the ship maneuverability, and the simulated results for the ship in the actual rivers will offer guidance on ship maneuvering in shallow waterways to guarantee safe navigation.

## 2. Numerical model of non-uniform flow

### 2.1. Basic equations and numerical computation

Basic equations of the numerical model of non-uniform flow contain continuity equation and momentum equations. In the Cartesian coordinates system, basic equations are expressed as follows.

#### (1) Continuity equation

$$\frac{\partial Z}{\partial t} + \frac{\partial}{\partial x}(hu) + \frac{\partial}{\partial y}(hv) = 0 \quad (1)$$

#### (2) Momentum equation in x direction

$$\frac{\partial u}{\partial t} + u \frac{\partial u}{\partial x} + v \frac{\partial u}{\partial y} + g \frac{\partial Z}{\partial x} + g \frac{n^2 u \sqrt{u^2 + v^2}}{h^{4/3}} - v \left( \frac{\partial^2 u}{\partial x^2} + \frac{\partial^2 u}{\partial y^2} \right) - f_e v = 0 \quad (2)$$

#### (3) Momentum equation in y direction

$$\frac{\partial v}{\partial t} + u \frac{\partial v}{\partial x} + v \frac{\partial v}{\partial y} + g \frac{\partial Z}{\partial y} + g \frac{n^2 v \sqrt{u^2 + v^2}}{h^{4/3}} - u \left( \frac{\partial^2 v}{\partial x^2} + \frac{\partial^2 v}{\partial y^2} \right) + f_e u = 0 \quad (3)$$

Due to the irregular banks of natural rivers, thus, the method of mesh fitting river bank is adopted for overcoming the issue of largely fluctuating river bank. The body-fitted curvilinear coordinate system has been widely used for calculating the flow around arbitrary complex bodies, thus, which was employed for this study. Typically, the conversion equations in the body-fitted curvilinear coordinate system are given by the following equation.

$$\begin{cases} \alpha \frac{\partial^2 x}{\partial \xi^2} + \gamma \frac{\partial^2 x}{\partial \eta^2} + J^2 \left( P \frac{\partial x}{\partial \xi} + Q \frac{\partial x}{\partial \eta} \right) = 0 \\ \alpha \frac{\partial^2 y}{\partial \xi^2} + \gamma \frac{\partial^2 y}{\partial \eta^2} + J^2 \left( P \frac{\partial y}{\partial \xi} + Q \frac{\partial y}{\partial \eta} \right) = 0 \end{cases} \quad (4)$$

In Eq. (4),  $P$  and  $Q$  are adjustable factors,  $\alpha = x_\eta^2 + y_\eta^2$ ,  $\gamma = x_\xi^2 + y_\xi^2$ , and  $J = x_\xi y_\eta - x_\eta y_\xi$ . After the coordinate transformation, basic equations in the body-fitted curvilinear coordinates system can be expressed as follows.

#### (1) Continuity equation

$$\frac{\partial Z}{\partial t} + \frac{1}{C_\xi C_\eta} \frac{\partial}{\partial \xi}(hu_\xi C_\eta) + \frac{1}{C_\xi C_\eta} \frac{\partial}{\partial \eta}(hv_\eta C_\xi) = 0 \quad (5)$$

#### (2) Momentum equation in $\xi$ direction

$$\begin{aligned} \frac{\partial u_\xi}{\partial t} + \frac{1}{C_\xi C_\eta} \left[ \frac{\partial}{\partial \xi}(C_\eta u_\xi^2) + \frac{\partial}{\partial \eta}(C_\xi u_\xi v_\eta) + u_\xi v_\eta \frac{\partial C_\eta}{\partial \eta} - v_\eta^2 \frac{\partial C_\eta}{\partial \xi} \right] + g \frac{1}{C_\xi} \frac{\partial Z}{\partial \xi} \\ + g \frac{n^2 u_\xi \sqrt{u_\xi^2 + v_\eta^2}}{h^{4/3}} - \frac{1}{C_\xi C_\eta} \left[ \frac{\partial}{\partial \xi}(C_\eta \sigma_{\xi\xi}) + \frac{\partial}{\partial \eta}(C_\xi \sigma_{\eta\xi}) + \sigma_{\xi\eta} \frac{\partial C_\xi}{\partial \eta} - \sigma_{\eta\xi} \frac{\partial C_\eta}{\partial \xi} \right] = 0 \end{aligned} \quad (6)$$

#### (3) Momentum equation in $\eta$ direction

$$\begin{aligned} \frac{\partial v_\eta}{\partial t} + \frac{1}{C_\xi C_\eta} \left[ \frac{\partial}{\partial \xi}(C_\eta u_\xi v_\eta) + \frac{\partial}{\partial \eta}(C_\xi v_\eta^2) + u_\xi v_\eta \frac{\partial C_\eta}{\partial \xi} - u_\xi^2 \frac{\partial C_\xi}{\partial \xi} \right] + g \frac{1}{C_\eta} \frac{\partial Z}{\partial \eta} \\ + g \frac{n^2 v_\eta \sqrt{u_\xi^2 + v_\eta^2}}{h^{4/3}} - \frac{1}{C_\xi C_\eta} \left[ \frac{\partial}{\partial \xi}(C_\eta \sigma_{\xi\eta}) + \frac{\partial}{\partial \eta}(C_\xi \sigma_{\eta\eta}) + \sigma_{\eta\xi} \frac{\partial C_\eta}{\partial \xi} - \sigma_{\xi\xi} \frac{\partial C_\xi}{\partial \eta} \right] = 0 \end{aligned} \quad (7)$$

where  $\xi$  and  $\eta$  are two coordinates in the curvilinear coordinate system,  $u_\xi$  is the flow velocity in the direction of  $\xi$ ,  $v_\eta$  is the flow velocity in the direction of  $\eta$ , and  $Z$  and  $h$  are the water level and water depth, respectively;  $C_\xi$  and  $C_\eta$  are the Lamé coefficients in curvilinear coordinates, where  $C_\xi = \sqrt{x_\xi^2 + y_\xi^2}$  and  $C_\eta = \sqrt{x_\eta^2 + y_\eta^2}$ .  $\sigma_{\xi\xi}$ ,  $\sigma_{\xi\eta}$ ,  $\sigma_{\eta\xi}$ , and  $\sigma_{\eta\eta}$  are the turbulent shear stresses.

$$\sigma_{\xi\xi} = 2v_t \left[ \frac{1}{C_\xi} \frac{\partial u_\xi}{\partial \xi} + \frac{v_\eta}{C_\xi C_\eta} \frac{\partial C_\xi}{\partial \eta} \right]$$

$$\sigma_{\eta\eta} = 2v_t \left[ \frac{1}{C_\eta} \frac{\partial v_\eta}{\partial \eta} + \frac{u_\xi}{C_\xi C_\eta} \frac{\partial C_\eta}{\partial \xi} \right]$$

$$\sigma_{\xi\eta} = \sigma_{\eta\xi} = v_t \left[ \frac{C_\eta}{C_\xi} \frac{\partial}{\partial \xi} \left( \frac{v_\eta}{C_\eta} \right) + \frac{C_\xi}{C_\eta} \frac{\partial}{\partial \eta} \left( \frac{u_\xi}{C_\xi} \right) \right]$$

$$\sigma_{\xi\eta} = \sigma_{\eta\xi} = v_t \left[ \frac{C_\eta}{C_\xi} \frac{\partial}{\partial \xi} \left( \frac{v_\eta}{C_\eta} \right) + \frac{C_\xi}{C_\eta} \frac{\partial}{\partial \eta} \left( \frac{u_\xi}{C_\xi} \right) \right]$$

Eqs. (5)–(7) are similar in the form, and can be formulated into a common format. Only a general Fortran program is necessary for Eq. (8), and then basic equations can be solved by employing the general program.

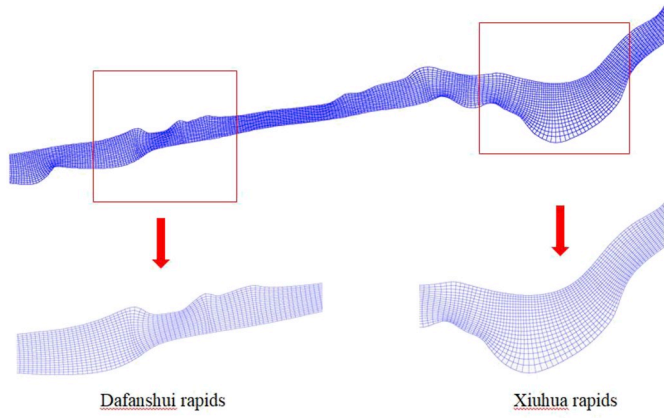


Fig. 1. Computational grids of part of the study reach.

$$C_\xi C_\eta \frac{\partial \varphi}{\partial t} + \frac{\partial(C_\eta u_\xi \varphi)}{\partial \xi} + \frac{\partial(C_\xi v_\eta \varphi)}{\partial \eta} = \frac{\partial}{\partial \xi} \left( \Gamma \frac{C_\eta}{C_\xi} \frac{\partial \varphi}{\partial \xi} \right) + \frac{\partial}{\partial \eta} \left( \Gamma \frac{C_\xi}{C_\eta} \frac{\partial \varphi}{\partial \eta} \right) + C \quad (8)$$

Basic equations in body-fitted curvilinear coordinate system are solved through the SIMPLEC algorithm (Doormaal and Raithby, 1984). Firstly, the relevant coefficients of coordinate transformation are calculated, as well as the computation of initial water depth of the whole study reach based on the upper and lower boundary conditions. Velocity in the direction of the two curvilinear coordinates is solved based on momentum equations. Water depth of the study reach is calculated and modified along with the velocity. Finally, the above steps are repeated until solving convergence, except the computation of coefficients of coordinate transformation. In the process of differential discretization and the solution of basic equations, the staggered-grid method is

adopted, for the purpose of overcoming the difficulty of discretizing the pressure gradient term and continuity equation. Besides, sub-relaxation technique is used aiming to promote the convergence of the non-linear iteration. The tridiagonal matrix algorithm (TDMA) is applied to the solution of difference equations. The basis for convergence is that the error of continuous equation is less than the given value.

### 2.2. Validation of the numerical model of non-uniform flow

Measured data of the water level ( $Z$ ) and flow velocity ( $V_F$ ) in a small reach of the Lancang River are selected to validate the reliability of the numerical model of non-uniform flow. The average measured flow discharge at the reach on May 15, 2016 was approximately  $1635 \text{ m}^3 \text{ s}^{-1}$ , which was selected as the computational flow discharge to validate  $Z$  and  $V_F$ . The reach for the validation of  $Z$  is below the Jinghong dam, till the end of the No.243 boundary stele, about 76 km, and grids used to discretize were curvilinear grids. The study reach includes about 40000 grids, and average length and width of the grid are about 19 m and 15 m, respectively. River width at the validated reach changes greatly, and the width of the local position is less than 100 m in the dry season, while more than 100 m in the flood season. The Jinghong dam is located about 5 km north of JingHong city, Yunnan province, China, and it is the sixth of eight cascade power stations in the lower reaches of the Lancang River. The No.243 boundary stele is located at the entrance of the Lancang River into Myanmar. Cross-sections for the validation of  $V_F$  are located at the Dafanshui and Xiuhua rapids, and computational grids of two rapids are presented in Fig. 1. Dafanshui and Xiuhua rapids are located at 70.3 km and 68.3 km downstream of the Jinghong dam, respectively. Results are shown in Fig. 2 and Fig. 3, respectively.  $L_b$  is the distance from the No.243 boundary stele, and  $L_w$  is the distance of cross-section in the direction of river width. Computed values are in good agreement with the measured data, indicating that the numerical model

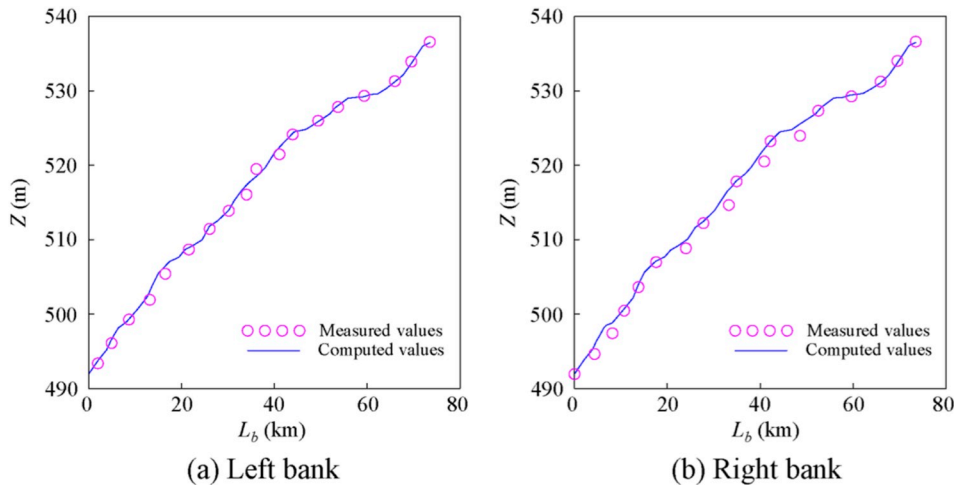


Fig. 2. Validation of water level.

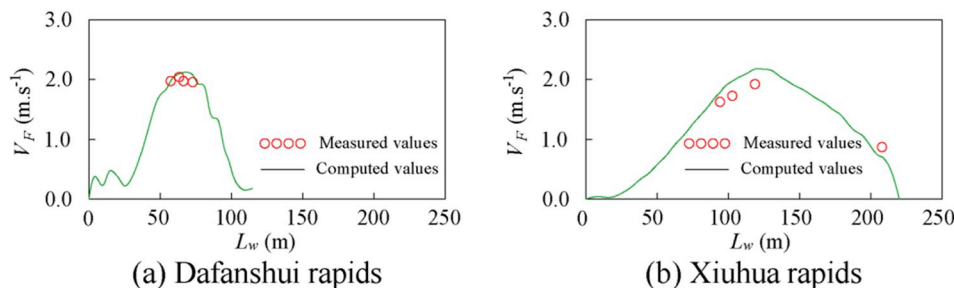


Fig. 3. Validation of flow velocity.

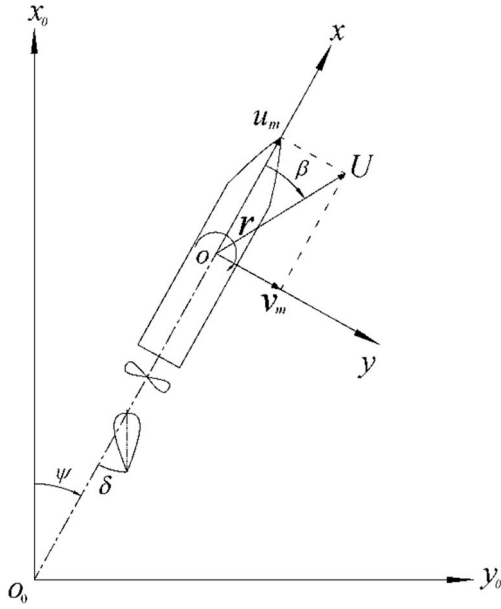


Fig. 4. Coordinate systems.

of non-uniform simulates the flow motion well.

### 3. Numerical model of ship maneuvering in deep and open water

#### 3.1. Coordinate systems

Fig. 4 shows the coordinate systems implemented in this study: the spatial fixed coordinate system  $o_0 - x_0y_0z_0$ , where the  $x_0 - y_0$  plane coincides with the still-water surface and the  $z_0$  axis points vertically downward; and the moving ship-fixed coordinate system  $o - xyz$ , where  $o$  is taken at the midship of the ship, and the  $x$ ,  $y$ , and  $z$  axes point toward the bow of the ship, starboard, and vertically downward, respectively. The heading angle  $\psi$  is defined as the angle between  $x_0$  and  $x$  axes,  $\delta$  is the rudder angle, and  $r$  is the yaw rate. Additionally,  $u_m$  and  $v_m$  denote the ship speed components in the directions of  $x$  and  $y$ , respectively. The drift angle at midship position  $\beta$  is defined as  $\beta = \tan^{-1}(v_m/u_m)$ , and the total velocity  $U$  is defined as  $U = \sqrt{u_m^2 + v_m^2}$ .

#### 3.2. Still- and deep-water motion equations

Modeling the actual motion of a ship with six degrees of freedom is very complicated. Generally the maneuvering motions of a ship in still and deep water are represented in terms of the surge, sway, and yaw need to be considered while the roll, pitch (or trim), and heave motion can be ignored from a practical point of view. The motion equations are expressed as

$$\left. \begin{aligned} (m + m_x)\dot{u}_m - (m + m_y)v_m r &= X_H + X_R + X_P \\ (m + m_y)\dot{v}_m + (m + m_x)u_m r &= Y_H + Y_R + Y_P \\ (I_{zG} + J_z)\dot{r} &= N_H + N_R + N_P \end{aligned} \right\} \quad (9)$$

Subscripts  $H$ ,  $P$  and  $R$  mean the hull, propeller, and rudder, respectively. The lateral force component and moment are neglected here because their values are relatively small, consequently, these two parameters are thus incorporated into the propeller-influenced hull force calculation in the MMG-based model.  $Y_P$  and  $N_P$  are expressed as follows:

$$Y_P = 0, N_P = 0 \quad (10)$$

#### 3.2.1. Hydrodynamic forces acting on ship hull

Surge force  $X_H$ , lateral force  $Y_H$ , yaw moment  $N_H$  around midship acting on ship hull are expressed as follows:

$$\left. \begin{aligned} X_H &= (1/2)\rho L d U^2 X'_H \\ Y_H &= (1/2)\rho L d U^2 Y'_H \\ N_H &= (1/2)\rho L^2 d U^2 N'_H \end{aligned} \right\} \quad (11)$$

where  $v'_m$  represents the non-dimensionalized lateral velocity defined as  $v_m/U$ , and  $r'$  is the non-dimensionalized yaw rate defined as  $rL/U$ .

Based on the resistance theory of the cross-flow, calculation formulas of  $X'_H$ ,  $Y'_H$  and  $N'_H$  was put forward by Inoue et al. (1981) and can be expressed as follows:

$$\left. \begin{aligned} X'_H &= X'(u'_m) + X'_{v_m v_m} v_m'^2 + X'_{v_m r} v'_m r' + X'_{r r} r'^2 \\ Y'_H &= Y'_{v_m} v'_m + Y'_r r' + Y'_{v_m v_m} |v'_m| v'_m + Y'_{v_m r} |r'| v'_m + Y'_{r r} |r'| r' \\ N'_H &= N'_{v_m} v'_m + N'_r r' + N'_{v_m v_m} |v'_m| v'_m + N'_{v_m r} v'_m r'^2 \end{aligned} \right\} \quad (12)$$

where  $X'_{v_m v_m}$ ,  $X'_{v_m r}$ ,  $X'_{r r}$ ,  $Y'_{v_m}$ ,  $Y'_r$ ,  $Y'_{v_m v_m}$ ,  $Y'_{v_m r}$ ,  $Y'_{r r}$ ,  $N'_{v_m}$ ,  $N'_r$ ,  $N'_{v_m v_m}$ ,  $N'_{v_m r}$  and  $N'_{r r}$  are called the hydrodynamic derivatives on maneuvering, Xin-le et al. (1999) provides detail calculation methods of the hydrodynamic derivatives.

#### 3.2.2. Propeller-induced hydrodynamic force

In the MMG model, surge force due to propeller  $X_P$  can be expressed as follows:

$$X_P = (1 - t_p)T \quad (13)$$

For simplicity, the thrust deduction coefficient  $t_p$  is assumed to be constant for a given propeller load. Propeller thrust  $T$  is written as

$$T = \rho n_p^2 D_p^4 K_T(J_P) \quad (14)$$

The thrust coefficient  $K_T$  can be derived by 2nd-order polynomial fitting, as follows.

$$K_T(J_P) = k_2 J_P^2 + k_1 J_P + k_0 \quad (15)$$

The advanced ration  $J_P$  is defined as follows:

$$J_P = \frac{u_m(1 - w_p)}{n_p D_p} \quad (16)$$

where  $n_p$  and  $D_p$  are the revolution speed and diameter of the propeller, respectively.  $w_p$  is the wake fraction changing with maneuvering motions in general. Several formulae for  $w_p$  have been summarized by Yasukawa and Yoshimura (2015). In this study the following formula is used

$$w_p = w_{p0} \exp(-8\beta_p^2) \quad (17)$$

where  $w_{p0}$  is the wake fraction when the ship is advancing straightforward, and  $\beta_p$  is the geometrical inflow angle to the propeller, which can be expressed as follows:

$$\beta_p = \beta - x'_p r' \quad (18)$$

Here,  $x'_p$  denotes the non-dimensional longitudinal coordinate of propeller position.

In the expression of  $X_P$ , the steering effect on the propeller thrust is excluded. Instead, this effect is taken into account via the rudder force component, as is described in the next section.

#### 3.2.3. Hydrodynamic forces induced by steering

Effective rudder forces  $X_R$ ,  $Y_R$  and  $N_R$  are expressed as

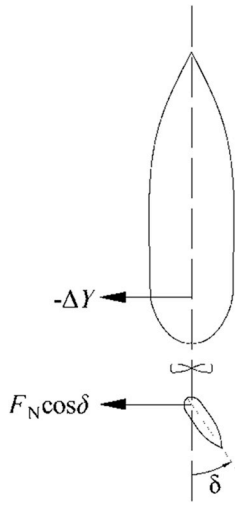


Fig. 5. Schematic figure of rudder force and the additional lateral force induced by steering.

$$\left. \begin{aligned} X_R &= -(1 - t_R)F_N \sin \delta \\ Y_R &= -(1 + a_H)F_N \cos \delta \\ N_R &= -(x_R + a_H x_H)F_N \cos \delta \end{aligned} \right\} \quad (19)$$

where  $F_N$  is normal force on the rudder. Note that tangential force on the rudder is neglected in Eq. (19).  $t_R$ ,  $a_H$ , and  $x_H$  are the coefficients that primarily represent the hydrodynamic interactions between the ship hull and rudder. The  $t_R$  is the steering resistance deduction coefficient, as it defines the deduction coefficient of rudder resistance versus  $F_N \sin \delta$ , which is the longitudinal component of  $F_N$ . It should be noted that  $X_R$  includes a component of the propeller thrust change owing to steering as mentioned in subsection 3.2.2. Therefore,  $t_R$  is a coefficient of both the rudder resistance deduction and the propeller thrust increase induced by steering. The underlying reason steering-induced propeller thrust increase occurs as a result of an increase of the nominal wake at the propeller position is not clear at present; however, it is suggested that the tangential force component on the rudder neglected in Eq. (20) may involve in  $t_R$ .

The  $a_H$  and  $x_H$  are the rudder force increase factor and the position of an additional lateral force component, respectively. The  $a_H$  represents the factor of steering-induced lateral force acting on the ship hull versus  $F_N \cos \delta$  which is the lateral component of  $F_N$ . The  $x_H$  means the longitudinal acting point of the additional lateral force component. The measured value of  $x_H$  was about  $-0.45L$ , and the additional lateral force was found to act on the stern portion of the hull. The phenomena may be understood by considering the hydrodynamic interaction of a wing with a flap. The ship hull and rudder are regarded as the main wing and the flap, respectively, as is shown in Fig. 5. The lift force, lateral force in this case, is induced on the rudder by steering, while an additional force component,  $\Delta Y$  in Fig. 5, is induced on the ship hull;  $\Delta Y$  is a product of the hydrodynamic interaction between the hull (main wing) and rudder (flap). Then,  $a_H$  is defined by  $-\Delta Y/F_N \cos \delta$ , and  $x_H$  can be regarded as the acting point of  $\Delta Y$ .

Eq. (19) is not theoretically derived,  $(1 - t_R)$  is given by the regression analysis (Xin-le et al., 1999) as follows:

$$(1 - t_R) = 0.7382 - 0.0539C_b + 0.1755C_b^2 \quad (20)$$

The normal force  $F_N$  of the rudder is expressed as follows:

$$F_N = (1/2)\rho A_R U_R^2 f_\alpha \sin \alpha_R \quad (21)$$

where  $f_\alpha$  is the rudder lift gradient coefficient, which can be estimated by using Fujii's formula, and is commonly applied as follows:

$$f_\alpha = \frac{6.13\lambda_R}{\lambda_R + 2.25} \quad (22)$$

Here,  $\lambda_R$  represents the aspect ratio of the rudder.

The resultant inflow velocity to rudder  $U_R$  is expressed as follows:

$$U_R = \sqrt{U^2(1 - w_R)^2 \{1 + KG(s)\}} \quad (23)$$

In Eq. (23),  $w_R$  is obtained via the following formula:

$$w_R = w_{R0} \cdot w_P / w_{P0}$$

where the magnitude of  $w_{R0}$  is approximated as 0.25, and  $K$  is obtained via the following formula (Xin-le et al., 1999):

$$K = \begin{cases} 1.065, & \delta \geq 0 \\ 0.935, & \delta < 0 \end{cases}$$

The effective inflow angle to the rudder  $\alpha_R$  can be calculated via the following formula:

$$\alpha_R = \delta - \gamma_R \beta_R \quad (24)$$

In Eq. (24),  $\beta_R = \beta - 2x'_R r'$ , where  $x'_R \approx -0.5$ .

### 3.3. Motion equations for deep-water flow motion

When a ship is sailing in flowing water,  $V_F$  is the absolute flow velocity of the ship's position and can be calculated mainly including two steps. Firstly, coordinates of the ship are searched in flow field by the basic function in finite element method, and then  $V_F$  is obtained by interpolating the flow velocity at four nodes of the grid.  $\psi_F$  is the flow direction in the spatial fixed coordinate system.  $u_{cx}$  and  $u_{cy}$  denote the absolute flow velocity components in the directions of  $x$  and  $y$ , respectively.  $u_{cx}$  and  $u_{cy}$  are expressed as

$$\left. \begin{aligned} u_{cx} &= V_F \cos(\psi_F - \psi) \\ u_{cy} &= V_F \sin(\psi_F - \psi) \end{aligned} \right\} \quad (25)$$

Ship speeds relative to the flow in the direction of  $x$  and  $y$  can be expressed as

$$\left. \begin{aligned} u_m &= u_x - u_{cx} = u_x - V_F \cos(\psi_F - \psi) \\ v_m &= u_y - u_{cy} = u_y - V_F \sin(\psi_F - \psi) \end{aligned} \right\} \quad (26)$$

Taking the derivative of Eq. (26),

$$\left. \begin{aligned} \dot{u}_m &= \dot{u}_x - V_F r \sin(\psi_F - \psi) \\ \dot{v}_m &= \dot{u}_y + V_F r \cos(\psi_F - \psi) \end{aligned} \right\} \quad (27)$$

By substituting Eqs. (26)–(27) into Eq. (9), the following equations are obtained:

$$\left. \begin{aligned} (m + m_x)\dot{u}_x &= X + (m + m_y)u_y r + (m_x - m_y)V_F r \sin(\psi_F - \psi) \\ (m + m_y)\dot{u}_y &= Y - (m + m_x)u_x r + (m_x - m_y)V_F r \cos(\psi_F - \psi) \\ (I_{zG} + J_z)\dot{r} &= N \end{aligned} \right\} \quad (28)$$

Eq. (28) shows the ship lateral motion equations for deep-water flow motion.

### 3.4. Solutions of ship maneuvering motion equations

Ordinary differential equations with first order derivatives will not be difficult to solve, but analytical solutions will hardly be obtained. Runge–Kutta method has been very much common tool to get numerical solutions. Thus, in this study, the fourth-order Runge–Kutta method is adopted to solve the ship maneuvering motion equations. Variables of the ship maneuvering motion equations are  $u_x$ ,  $u_y$ , and  $r$ . Given that the initial condition is expressed as

**Table 1**  
Main parameters of the Baoshou21.

Main parameters	Units	Value	Main parameters	Units	Value
Displacement	t	595.6	Prismatic coefficient		0.761
Ship length	m	52.6	Rudder area	m <sup>2</sup>	2.5 × 2
Ship width	m	8.3	Propeller diameter	m	1.47
Designed draft	m	1.95	Propeller pitch	m	1.103
Designed speed	m.s <sup>-1</sup>	6.05	Propeller number		2
Block coefficient		0.749			

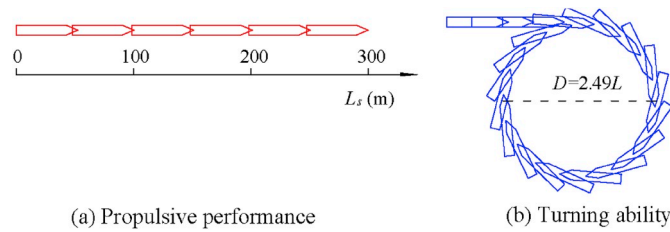


**Fig. 6.** Verification test of propulsive performance and turning ability.

$$\left. \begin{aligned} u_x &= u_{x0} \\ u_y &= u_{y0} \\ r &= r_0 \end{aligned} \right\}$$

Eq. (28) is modified as follows:

$$\left. \begin{aligned} \dot{u}_x &= \left[ X + (m + m_y)u_y r + (m_x - m_y)V_{Fr} \sin(\psi_F - \psi) \right] / (m + m_x) \\ \dot{u}_y &= \left[ Y - (m + m_x)u_x r + (m_x - m_y)V_{Fr} \cos(\psi_F - \psi) \right] / (m + m_y) \\ \dot{r} &= N / (I_{zG} + J_z) \end{aligned} \right\} \quad (29)$$

Assuming Eq. (29) can be rewritten as Eq. (30),

$$\left. \begin{aligned} \dot{u}_x &= f_1(t, u_x, u_y, r) \\ \dot{u}_y &= f_2(t, u_x, u_y, r) \\ \dot{r} &= f_3(t, u_x, u_y, r) \end{aligned} \right\} \quad (30)$$

by implementing the general form of the Runge–Kutta method, the solution of Eq. (30) can be expressed as

$$\left. \begin{aligned} u_{x,i+1} &= u_{xi} + \frac{\Delta t}{6}(a_1 + 2a_2 + 2a_3 + a_4) \\ u_{y,i+1} &= u_{yi} + \frac{\Delta t}{6}(b_1 + 2b_2 + 2b_3 + b_4) \\ r_{i+1} &= r_i + \frac{\Delta t}{6}(c_1 + 2c_2 + 2c_3 + c_4) \end{aligned} \right\} \quad (31)$$

Because the expression for  $a_1, b_1, c_1, a_2, b_2, c_2, a_3, b_3, c_3, a_4, b_4$  and  $c_4$  are too verbose, they are not presented here. After the above parameters are obtained, the location of a ship at any moment, in addition to all related parameters, may be determined by solving the set of equations presented as Eq. (32).

$$\left. \begin{aligned} x_{i+1} &= x_i + (u_{xi} \cos\psi_i - u_{yi} \sin\psi_i)\Delta t \\ y_{i+1} &= y_i + (u_{xi} \sin\psi_i + u_{yi} \cos\psi_i)\Delta t \\ \psi_{i+1} &= \psi_i + r_i \Delta t \\ v_{x,i+1} &= u_{x,i+1} - V_F \cos(\psi_F - \psi_{i+1}) \\ v_{y,i+1} &= u_{y,i+1} - V_F \sin(\psi_F - \psi_{i+1}) \end{aligned} \right\} \quad (32)$$

### 3.5. Validation of the numerical model of ship maneuvering

Validation of the numerical model is performed on a cargo ship (Baoshou21) sailing in the Lancang River, and main parameters of the Baoshou21 are presented in Table 1.

Propulsive performance and turning ability of the Baoshou21 are evaluated by implementing its specifications and parameters in the numerical model of ship maneuvering motion. The test environment is an imaginary and unlimitedly wide water area, not the actual channel, and has uniform water depth. Water depth of verification tests is 2.5

**Table 2**  
Main parameters of the Huapinghao.

Main parameters	Units	Value	Main parameters	Units	Value
Displacement	t	405	Block coefficient		0.724
Ship length	m	46.2	Prismatic coefficient		0.690
Ship width	m	7.6	Propeller diameter	m	1.124
Designed draft	m	1.75	Propeller pitch	m	0.933
Designed speed	m.s <sup>-1</sup>	6.11			

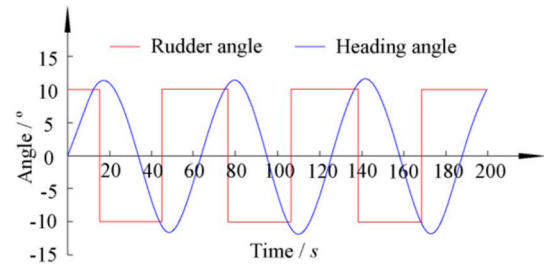


**Fig. 7.** Time histories curve of rudder and heading angles during 10°/10° Zig-Zag motion verification test (HuaPingHao).

**Table 3**  
The measured and computed values of  $K'$  and  $T'$ .

Items	Measured values	Computed values	Error (%)
$K'$	0.932	0.877	5.9
$T'$	0.540	0.511	5.4

times designed draft, namely  $h = 2.5d$ , and test time of propulsive performance and turning ability are 50 s and 100 s, respectively. The results are shown in Fig. 6.

The verification of propulsive performance aims to check whether the designed speed of the ship is reasonable or not, and the ship trajectory in the still water is a straight line or not. From the sailing distance within 50s and the ship trajectory in Fig. 6(a), it can be seen that the speed and trajectory predictions are reasonable. From previous researches (Xiu-heng and Wu, 1998; Xin-le et al., 1999), turning diameter  $D$  of the inland cargo ship with better turning ability is 1.5–3.5 times the ship length  $L$ , namely  $D = 1.5L\text{--}3.5L$ . Fig. 6(b) shows that the simulation result is consistent with the previous research. Considering this, it is reasonable to implement the ship-maneuvering numerical model proposed in this article to calculate the propulsive performance and turning ability of the representative ship (Baoshou 21).

Another ship (Huapinghao) sailing in the Lancang River was selected as the representative ship for the zig-zag motion verification test because the Baoshou 21 did not conduct the zig-zag motion verification testing. Some important parameters of the Huapinghao are presented in Table 2. The test water area of zig-zag motion is selected in the Ganlan dam water area of the Lancang River. The Ganlan dam water area, with slow flow velocity, and the width ranges from 170 m to 250 m. Water surface is gentle and longitudinal slope is about 0.4%. Water depth is approximately 10 m, about six times the designed draft depth of the ship. Generally speaking, the flow velocity, width and longitudinal slope of the water area meet the requirements of zig-zag motion test.

Fig. 7 shows the time history curves for the rudder and heading angles during 10°/10° zig-zag motion verification testing for load and rotational speed ratios of 90% each.  $K'$  and  $T'$  are the turning ability index and steering quality index, respectively. As is shown in Table 3, the computed values of  $K'$  and  $T'$  are in good agreement with the measured values in practice in such the river, therefore, it is reasonable to utilize the ship-maneuvering numerical model proposed in this article to perform numerical simulations of zig-zag motion.

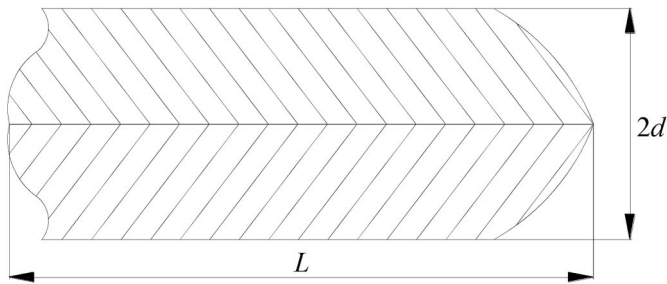


Fig. 8. Schematic diagram of ship hull supposed as a wing.

#### 4. Numerical model of ship maneuvering motion in shallow water

Incorporating the shallow water effect into the numerical model of ship maneuvering motion is primarily achieved by correcting the hydrodynamic derivatives of the model in deep water. Consequently, the motion equation is unaltered from Eq. (9), but values of the relevant coefficients are different.

##### 4.1. Added mass and added moment of inertia

Currently, there are three methods for calculating added mass and added moment of inertia, including slender-body theory method, singularity distribution method and the finite element method. Slender body theory method belongs to two-dimensional calculations. Although the proposed method is simple, there are noticeable error between the experimental and simulation results. Singularity distribution method and the finite element method are both three-dimensional fluid dynamics methods, however, the computational process is exceedingly complex. In summary, for the purpose of improving the accuracy of calculation and simplifying calculation, added mass and added inertia moment are calculated via a regression formula (Mei-qing, 1988). The regression formula is derived from large numbers of experimental data, which are expressed as

$$\left. \begin{aligned} \frac{m_{xh}}{m_{x\infty}} &= \left[ \left( \frac{h}{d} - 1 \right)^{1.3} + 3.77 + 1.14 \frac{B}{d} - 0.233 \frac{L}{d} - 3.43 C_b \right] / \left( \frac{h}{d} - 1 \right)^{1.3} \\ \frac{m_{yh}}{m_{y\infty}} &= \left[ \left( \frac{h}{d} - 1 \right)^{0.82} + 0.413 + 0.0320 \frac{B}{d} + 0.0129 \left( \frac{B}{d} \right)^2 \right] / \left( \frac{h}{d} - 1 \right)^{0.82} \\ \frac{J_{zvh}}{J_{z\infty}} &= \left[ \left( \frac{h}{d} - 1 \right)^{0.82} + 0.413 + 0.0192 \frac{B}{d} + 0.00554 \left( \frac{B}{d} \right)^2 \right] / \left( \frac{h}{d} - 1 \right)^{0.82} \end{aligned} \right\} \quad (33)$$

##### 4.2. Longitudinal hydrodynamic force acting on ship hull

The longitudinal hydrodynamic force acting on the ship hull in shallow water is calculated by modifying the total resistance coefficient and the added resistance of straightforward motion (Wei-min et al., 1982). The total resistance coefficient in shallow water is corrected as

$$\frac{C_{th}}{C_{t\infty}} = A + \frac{B}{h/d} \quad (34)$$

where  $C_{th}$  and  $C_{t\infty}$  are the total resistance coefficients of the straightforward motion in shallow and deep water, respectively, and  $A$  and  $B$  are empirical coefficients obtained by the numerous ship model tests.

The added resistance formula (Xin-le et al., 1999) is expressed as

$$\frac{X'_{vmth}}{X'_{vmr\infty}} = 1 - 0.9879 \frac{d}{h} + 21.9123 \left( \frac{d}{h} \right)^2 - 73.8161 \left( \frac{d}{h} \right)^3 + 71.1409 \left( \frac{d}{h} \right)^4 \quad (35)$$

##### 4.3. Lateral hydrodynamic force and moment acting on the ship hull

If ship hull is supposed as a wing,  $L$  is equivalent to the wing's chord, and  $2d$  is treated as the wing's span, as is shown in Fig. 8. Thus, the aspect ratio  $\lambda$  is the ratio of its span to its mean chord. Then, taking  $2d$  as the wing's span aims to eliminate the influence of a free surface.

The aspect ratio is expressed as

$$\lambda = \frac{2d}{L}$$

and the effective aspect ratio is defined as follows:

$$\lambda_e = \frac{\lambda}{\frac{d}{2h} \lambda + \left( \frac{\pi d}{2h} \cot \frac{\pi d}{2h} \right)^q}$$

The lateral hydrodynamic force and dynamic moment acting on the ship in shallow water can be decomposed into the linear and nonlinear components (Hirano, 1985). The formula for calculating the linear hydrodynamic derivatives is expressed as

$$\left. \begin{aligned} Y'_{vmh} &= - \left( \frac{\pi}{2} \lambda_e + 1.4 C_b \frac{B}{L} \right), & q &= 2.3 \\ Y'_{rth} &= \frac{\pi}{4} \lambda_e, & q &= 0.7 \\ N'_{vmh} &= -\lambda_e, & q &= 1.7 \\ N'_{rth} &= -(0.54 \lambda_e - \lambda_e^2), & q &= 0.7 \end{aligned} \right\} \quad (36)$$

Here,  $q$  is a constant, and it is determined via numerous captive model tests.

The formula of the nonlinear hydrodynamic derivatives (Inoue et al., 1981) is expressed as

$$\left. \begin{aligned} Y'_{vmv_{mh}}/Y'_{vmv_{m\infty}} &= 1 + 14(d/h)^{3.5} \\ Y'_{rrh}/Y'_{rr\infty} &= 1 + 3(d/h)^{2.5} \\ Y'_{vmrth}/Y'_{vmr\infty} &= 1 + 3(d/h)^{2.5} \\ N'_{rrh}/N'_{rr\infty} &= 1 + 5(d/h)^{3.5} \\ N'_{vmv_{mrh}}/N'_{vmv_{mr\infty}} &= 1 + 6(d/h)^{2.5} \\ N'_{vmrth}/N'_{vmr\infty} &= 1 + 6(d/h)^{2.5} \end{aligned} \right\} \quad (37)$$

##### 4.4. Thrust and moment due to propeller

The calculation of the propeller-induced thrust and moment as the ship travels through shallow water is carried out by correcting the deep water thrust deduction factor  $t_p$  and the wake fraction  $\omega_p$  to those in shallow water.

Xin-le et al. (1999) corrected the thrust deduction coefficient  $t_p$  as the following formula:

$$\frac{(1-t_p)_h}{(1-t_p)_\infty} = \frac{1}{1 - 0.2(d/h) + 0.7295(d/h)^2} \quad (38)$$

and the wake fraction  $\omega_p$  is corrected as

$$\frac{(1-\omega_p)_h}{(1-\omega_p)_\infty} = \cos \left( 1.4 C_b \frac{d}{h} \right) \quad (39)$$

##### 4.5. Rudder force and moment

The steering resistance deduction factor  $t_R$  in shallow water can adopt the value in deep water, whereas the moment in shallow water is obtained by correcting the flow-straightening coefficient  $\gamma_R$  of the ship hull and propeller in deep water (Xin-le and Yan-sheng, 1999).

$$\frac{\gamma_{Rh}}{\gamma_{R\infty}} = 1 + 0.0161 \frac{d}{h} + 4.4222 \left(\frac{d}{h}\right)^2 - 4.9825 \left(\frac{d}{h}\right)^3 \quad (40)$$

#### 4.6. Navigation resistance

Navigation resistance is assumed to be made up of two independent components of resistance during the upward sailing, which can be expressed as  $R = R_V + R_J$ .  $R$ ,  $R_V$  and  $R_J$  are navigation resistance, flow resistance and slope resistance, respectively. Flow resistance is divided into frictional resistance  $R_f$  and residual resistance  $R_r$ . The former is mainly related to the Reynolds number, while the latter is related to the Froude number. Namely,  $R_V = R_f(R_e) + R_r(F_r)$ . Some scholars have carried out a detailed study on the calculation of navigation resistance, and the famous ЭИВАНКОВ method was proposed (Guan-lun, 2004). Relevant parameters in the ЭИВАНКОВ formula were obtained by combining results of the actual ship tests and the ship model tests, such as the friction coefficient, the reduction coefficient of ship cross-section and so on. The Baoshou 21 belongs to the power-driven ship, and its flow resistance is calculated by the following formula:

$$R_V = f_1 A_s V_s^{1.83} + \xi_1 C_b A_m V_s^{1.7+4F_r} \quad (41)$$

In Eq. (41),s

$$A_s = L_w (C_1 d + C_b B)$$

$$V_s = (1.15 \sim 1.3) V_{cp} + V_a$$

$$\xi_1 = \frac{17.7 C_b^{2.5}}{\left(\frac{L_w}{6B}\right)^3 + 2}$$

$$A_m = \beta_c B d$$

$$F_r = \frac{V_s}{\sqrt{g L_w}}$$

Here,  $f_1$  is friction coefficient of the power-driven ship, and the Baosou 21 is the steel ship, so  $f_1 = 0.17$ ;  $A_s$  is the wetted surface area of ship;  $L_w$  is the waterline length of ship;  $C_1$  is the coefficient (for the power-driven,  $C_1 = 1.8$ );  $B$  is the ship width;  $V_s$  is the ship sailing speed, which is modified due to taking account for the influence of shallow water and narrow channel.  $V_{cp}$  is the longitudinal surface mean flow velocity;  $V_a$  is the minimum sailing speed required for a ship to sail upward successfully under the action of resistance, and  $V_a = 0.3\text{--}0.5$  m.  $s^{-1}$ ;  $\xi_1$  is the coefficient of residual resistance;  $A_m$  is the area of midship section of ship wetted section;  $\beta_c$  is the reduction coefficient of ship cross-section (for the power-driven,  $\beta_c = 0.93$ );  $F_r$  is the Froude number. Slope resistance is expressed as

$$R_J = \alpha W J \quad (42)$$

$W$  is the tons of water that a ship displaces when it is fully loaded, and  $J$  is the mean water surface gradient,  $\alpha$  is the correction coefficient for the local increase of water surface gradient ( $\alpha = 1.1\text{--}1.2$ )

#### 4.7. Shallow-water ship-maneuvering motion simulation

As previously mentioned, the cargo ship (BaoShou21) is implemented as the representative ship in a series of simulations, i.e., straightforward motion, turning motion, and zig-zag motion. A series of simulations for varying depth-draft ratios, rudder angles and flow velocity aim to reveal the ship maneuverability in shallow water. It should be noted that these simulations are carried out in an imaginary and unrestricted water area, not the actual river, and designed speed of the representative ship is treated as the initial sailing speed in the calculation of these tests. Besides, it is not necessary to add the flow velocity for straightforward and zig-zag motion simulations, and whether to add the

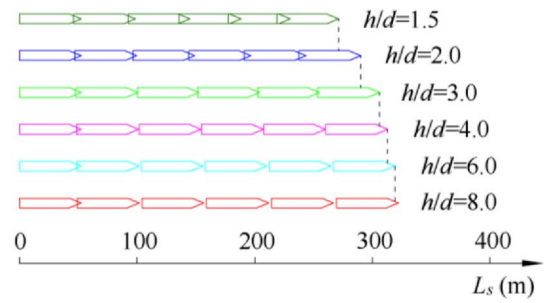


Fig. 9. Ship trajectories of straightforward motion.

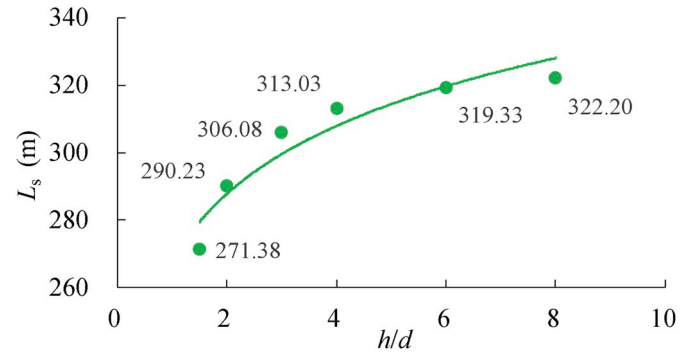


Fig. 10. Relation between the  $L_s$  and the  $h/d$ .

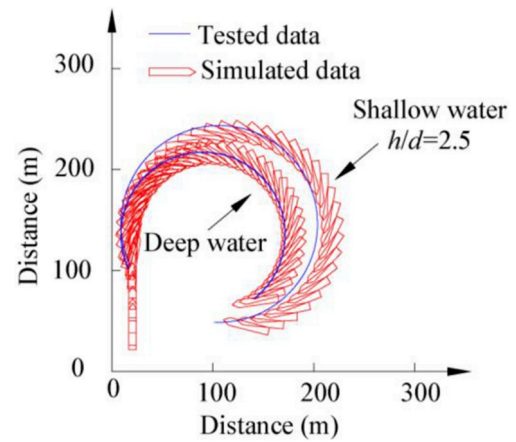


Fig. 11. Comparison of turning diameters between the tested data and simulated data.

flow velocity in turning motion simulation depends on the specific situation.

#### 4.8. Straightforward motion

Fig. 9 illustrates the straightforward motion ship trajectories for the same sailing time ( $t = 50$  s), the same rudder angle ( $\delta = 0^\circ$ ) and various depth-draft ratios ( $h/d = 1.5, 2.0, 3.0, 4.0, 6.0, 8.0$ ), and  $L_s$  is the sailing distance. Fig. 10 clearly reflects the relation between  $L_s$  and  $h/d$ . When the ship is traveling in shallow water ( $h/d < 3.0$ ), as the  $h$  decreases, the resistance rapidly increases as compared to deep-water travel; this results in a significantly shorter  $L_s$ .  $L_s$  tends to increase as the increase of  $h/d$ . However,  $L_s$  increases slowly when ship enters deep water ( $h/d \geq 3.0$ ). In this case, even if  $h/d$  increases continually, there is no obvious increase in  $L_s$  and tends to be stable. This finding demonstrates the significance of the shallow water effect, because, as resistance gradually

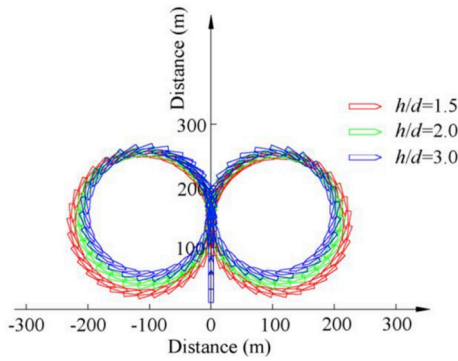


Fig. 12. Comparison of ship trajectories for various depth-draft ratio.

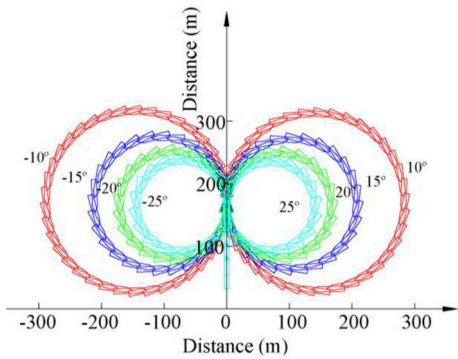


Fig. 13. Comparison of ship trajectories for various rudder angles.

decreases in deep water, the effect of water depth on  $L_s$  is greatly weakened.

#### 4.9. Turning motion

In order to verify the applicability of the proposed numerical model in turning motion of the actual ship, we conducted a turning test for the actual ship (Huapinghao). In the turning test and the numerical simulation in shallow water, water depth is 2.5 times the designed draft of the Huapinghao. The turning test is conducted in the Ganlan dam water area of the Lancang River. The conditions of numerical simulation are that initial heading angle and rudder angle are  $0^\circ$ , and the fixed rudder angle for ship turning motion is  $25^\circ$ . Fig. 11 shows the comparison of turning diameters of the actual ship and the model in shallow and deep water. Obviously, simulated trajectories are in good accordance with tested trajectories of the actual ship, indicating that the proposed numerical model based on the shallow water effect can apply to the simulation of the turning motion of the actual ship.

Fig. 12 shows a comparison of calculated turning trajectories for various depth-draft ratios ( $h/d = 1.5, 2.0, 3.0$ ). The results are obtained under the conditions that the flow velocity at the initial position of the ship, the initial heading angle, and the rudder angle are equal to zero; In addition, the fixed rudder angles for ship turning motion are  $15^\circ$  (right) and  $-15^\circ$  (left).

The turning diameter can be seen to increase as the water depth decreases. This is because the damping moment is increased when the ship is turning and yields a smaller yaw rate and drift angle in deep water. This smaller drift angle causes the turning speed to decrease. The above two factors result in a relatively increased turning diameter in shallow water, which is unfavorable for ship maneuverability in shallow waterways.

Fig. 13 shows the simulated turning trajectory results for various rudder angles ( $\delta = \pm 10^\circ, \pm 15^\circ, \pm 20^\circ, \pm 25^\circ$ ) and a fixed depth-draft ratio ( $h/d = 2.0$ ). The results are obtained under the conditions that the flow

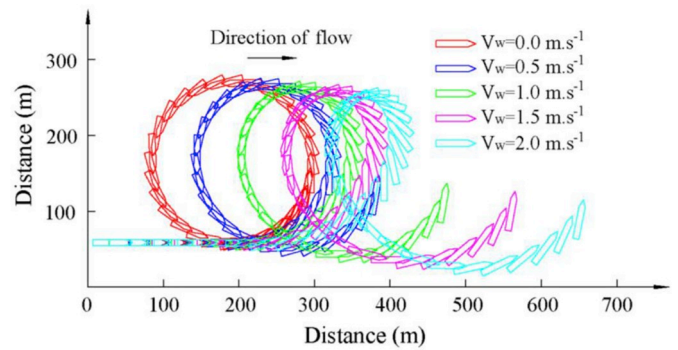


Fig. 14. Comparison of ship trajectories for various flow velocities.

velocity at the initial position of the ship, the initial heading angle, and the rudder angle are equal to zero. The larger rudder angle causes the turning diameter to decrease when the depth-draft ratio remains constant. The simulation results roughly agree with those obtained for deep water travel.

Fig. 14 compares the calculated turning trajectories for various flow velocities ( $V_w = 0.0, 0.5, 1.0, 1.5, 2.0 \text{ m s}^{-1}$ ) and a fixed depth-draft ratio ( $h/d = 2.0$ ). The results were obtained under the following conditions: initial heading angle and rudder angle are  $0^\circ$ , and a fixed rudder angle of ship turning motion is  $-15^\circ$ . The ship is turning and deflecting towards the direction of the flow when flow velocity exists. The results show that ship turning becomes increasingly abnormal as the flow velocity increases, with a complete circle becoming an arc with a smaller radius at higher flow velocities.

The proposed numerical model of ship-maneuvering motion, which is based on non-uniform flow and regression formulae on shallow water effect, is applied to a study on waterway regulation of the Dafanshui rapids and the Xiuhua rapids in the Lancang River. The Dafanshui rapids was narrow, and the channel width was about 60 m in the dry season. The channel width of the Xiuhua rapids was narrowed to 40 m due to the constructions of dikes.

Based on the navigation standard of inland waterway of China (Gang et al., 2014), the restricted waterway refers to the waterway producing obvious restriction for the navigation due to narrow water surface and small coefficient of cross-section  $C_c$ . Evaluation index of the restricted waterway is  $C_c$ . In general, if  $C_c > 10$ , the waterway is not the restricted waterway. In addition, cross-section coefficient of restricted waterway should be  $6 < C_c \leq 10$ .

$C_c$  can be calculated by the following formula:

$$C_c = A_c / A_m \quad (43)$$

$A_c$  is the flow area of cross-section of the waterway;  $A_m$  is area of midship section of ship wetted section and  $A_m = \beta_c B d$ ,  $\beta_c = 0.93$ .  $B$  is the ship width and  $d$  is the designed draft. For the Baoshou 21,  $A_m = 0.93 \times 8.3 \times 1.95 = 15.05 \text{ m}^2$ .

When the water levels of two rapids are the most unfavorable for ship navigation, for Dafanshui rapids,  $A_c$  is about  $396 \text{ m}^2$ ,  $C_c = 396 / 15.05 = 26.31 > 10$ ; for Xiuhua rapids,  $A_c$  is about  $168 \text{ m}^2$ ,  $C_c = 168 / 15.05 = 11.16 > 10$ . Therefore, the two study rapids do not belong to the restricted waterway.

The case-study simulation is completed in three general steps. At the first step, flow fields of the two rapids are calculated via the 2D flow numerical model proposed in the paper. And then, both of deep- and shallow-water simulations of ship-maneuvering motion are performed by incorporating flow field data into the calculations based on the proposed numerical model. At the final step, a comparison of ship trajectories in the deep and shallow water is performed to analyze the influence of reduced water depth on ship navigation resistance.

In the case of the Baoshou 21, since the minimum flow discharge of the JingHong power station should be controlled at  $800\text{--}1000 \text{ m}^3 \text{ s}^{-1}$  to

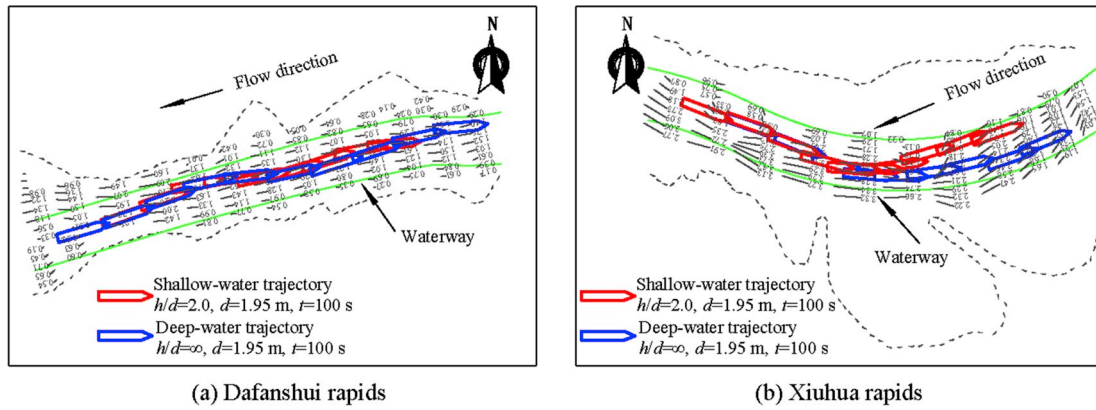


Fig. 15. Application of proposed numerical method to ship steering.

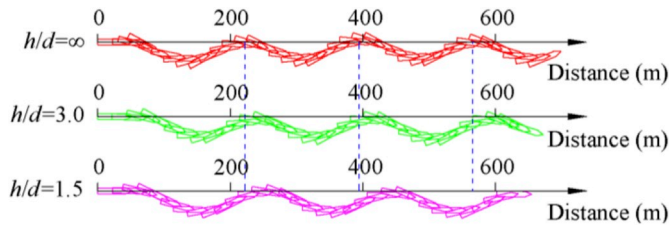


Fig. 16. Comparison of the 20°/20° zig-zag motion trajectories with various depth-draft ratio.

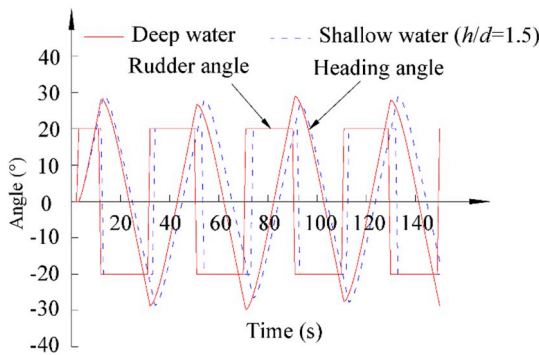


Fig. 17. Time histories of rudder and heading angles in shallow and deep water.

ensure the lowest navigable water level that would guarantee safe navigation of the fourth grade waterway. The lowest water depth of the fourth grade waterway is generally from 1.6 m to 1.9 m.  $800 \text{ m}^3 \text{ s}^{-1}$  serves as the most adverse flow condition, which is selected as the computational flow discharge for the purpose of ensuring safe navigation in this study. The initial speed required in the simulation is  $5.45 \text{ m s}^{-1}$ , and the heading angles are  $73^\circ$  and  $111^\circ$ , respectively, for deep and shallow water. Note that the same rudder angle is implemented for the same rapids in deep and shallow water. The trajectories of ship motion in deep and shallow water are shown in Fig. 15.

The flow velocity between the bottom of the ship and the riverbed is not only related the total bottom area of the ship, but also closely related to the water depth. When the ship is sailing in shallow water, the flow is divided and pushed along the two sides of the ship, leading to the increase of velocities along these two sides. Furthermore, the increased viscous resistance results in reduced travel distance in shallow water. This is also related to the flow field, because when the flow velocity is large, the viscous resistance is also large, thereby hindering forward movement.

#### 4.10. Zig-zag motion

Fig. 16 shows the results of simulating  $20^\circ/20^\circ$  zig-zag motion trajectories with various depth-draft ratios ( $h/d = 1.5, 3.0, \infty$ ). It can be seen that a smaller depth-draft ratio corresponds to a larger swing and period of zig-zag motion. This indicates that, under the influence of the shallow water effect, ship resistance increases and ship maneuverability decreases.

Time history curves for the rudder and heading angles during shallow and deep-water travel are shown in Fig. 17. Results show that the duration of zig-zag motion occurring in shallow water is longer than that occurring in deep water; this means that maneuverability is reduced in shallow water because of the lower water depth.

### 5. Conclusions

In this study, with the aim of investigating the ship maneuverability in shallow water a numerical model of ship maneuvering motion that takes account of the shallow water effect is proposed based on the MMG model. The flow field data solved based on a numerical model of non-uniform flow are taken as the basis for calculating hydrodynamic forces of the ship model. Simulations of straightforward, turning, and zig-zag motions in an unrestricted water area are performed on a cargo ship by using various empirical methods, the fourth-order Runge-Kutta method and Fortran programming language. Ship trajectories in shallow water for varying depth-draft ratio, rudder angle and flow velocity are compared, indicating that shallow water caused ships to increase its sailing resistance and to decrease its maneuverability. As the depth-draft ratio decreases, an increase in the duration of zig-zag motion means that shallow water effect is pronounced and ship maneuverability is reduced. Besides, the numerical result of turning motion is compared with the available experimental data, and reasonable agreement is achieved. The application of the ship model in an engineering case demonstrates it is reasonable to adopt the model considering the shallow water effect to simulate and guide maneuvering motions of the ship in mountainous river.

Ship maneuverability in shallow water will undoubtedly attract further attention of scientists and engineers, due to the rapid trend of enlargement in ship size in the world market. However, safety operations in inland waters, particularly, in mountainous rivers have yet completely insured. Study on ships in shallow waters should be continued to deepen the understanding of the phenomena, including the effects of non-uniform riverbed morphology, confined shallow water, inclined river bed, wind waves and tidal waves, and shallow water waves close to the critical ship speed, on ship operations.

## Acknowledgments

This work was partly supported by The National Key Research and Development Program of China (2016YFC0802204) and the Basic and Frontier Research Programs of Chongqing, China (cstc2018jcyjAX0534).

## References

- Barras, C., 2012. Ship Squat in Open Water and in Confined Channels (chapter 17).  
 Debaillon, P., 2010. Numerical investigation to predict ship squat. *J. Ship Res.* 54 (2), 133–140.  
 Delefortrie, G., Vantorre, M., 2007. Modeling the maneuvering behavior of container carriers in shallow water. *J. Ship Res.* 51 (4), 287–296.  
 Doormaal, J., Raithby, G., 1984. Enhancement of SIMPLE method for predicting incompressible fluid flows. *Numer. Heat Transf.* 7 (2), 147–163.  
 Du, P., Ouahsine, A., Sergent, P., 2018. Influences of the separation distance, ship speed and channel dimension on ship maneuverability in a confined waterway. *CR Mecanique* 346 (5), 390–401.  
 Gang, Fu, Ju-hai, Li, Hong-bo, Liu, 2014. Navigation Standard of Inland Waterway (GB 50139). <http://www.doc88.com/p-1595905762193.html>.  
 Gourlay, T.P., 2008. Slender-body methods for predicting ship squat. *J. Ocean Eng.* 35 (2), 191–200.  
 Guan-lun, Zhou, 2004. Manual of Waterway Engineering. China Communication Press.  
 He, S., Kellett, P., Yuan, Z., Incecik, A., Turan, O., Boulougouris, E., 2016. Manoeuvring prediction based on CFD generated derivatives. *J. Hydrodyn.* 28 (2), 284–292.  
 Hirano, M., 1985. An Experimental Study on Manoeuvring Hydrodynamic Forces in Shallow Water. Western shipbuilding association.  
 Inoue, S., Hirano, M., Kijima, K., 1981. Hydrodynamic derivatives on ship manoeuvring. *Int. Shipbuildg Prog.* 28, 207–209.  
 Lin-jia, Yang, Yi-han, Tao, 2013. CFD-based calculation of regular transverse wave force in the manoeuvring mathematical modeling group (MMG) model. *Appl. Mech. Mater.* 380–384, 1716–1720.  
 Maimun, A., Priyanto, A., Rahimuddin, Sian, A.Y., Awal, Z.I., Celement, C.S., et al., 2013. A mathematical model on manoeuvrability of a LNG tanker in vicinity of bank in restricted water. *Saf. Sci.* 53, 34–44.  
 Mei-qing, Li, 1988. Simulation and Comprehensive Evaluation of Ship Maneuverability under Multiple Working Conditions in Wind, Wave, Flow and Restricted Waterway (Ph.D. thesis of WUT).  
 Pacuraru, F., Domnisoru, L., 2017. Numerical investigation of shallow water effect on a barge ship resistance. *IOP Conf. Ser. Mater. Sci. Eng.* 227 (1), 1–8.  
 Petru, S.S., 2017. Numerical simulation of shallow waters effects on sailing ship “Mircea” hull. *Sci. Bull. Naval Acad.* 19 (2), 97–102.  
 Meng, Qing-jie, Wan, De-cheng, 2016. Numerical simulations of viscous flow around the obliquely towed KVLCC2M model in deep and shallow water. *J. Hydrodyn.* 28 (3), 506–518.  
 Razzgallah, I., Kaidi, S., Smaoui, H., Sergent, P., 2018. The impact of free surface modelling on hydrodynamic forces for ship navigating in inland waterways: water depth, drift angle, and ship speed effect. *J. Mar. Sci. Technol.* 109, 1–22.  
 Reichel, M., 2017. Prediction of manoeuvring abilities of 10000 DWT pod-driven coastal tanker. *J. Ocean Eng.* 136, 201–208.  
 Rotteveel, E., Van der Ploeg, A., Hekkenberg, R., 2017. Optimization of ships in shallow water with viscous flow computations and surrogate modeling. In: Proceedings of the 13th International Symposium on Practical Design of Ships and Other Floating Structures, pp. 1–8.  
 Sutulo, S., Rodrigues, J.M., Guedes, S.C., 2010. Hydrodynamic characteristics of ship sections in shallow water with complex bottom geometry. *J. Ocean Eng.* 37 (10), 947–958.  
 Terziev, M., Tezdogan, T., Oguz, E., Gourlay, T., Demirel, Y.K., Incecik, A., 2018. Numerical investigation of the behaviour and performance of ships advancing through restricted shallow waters. *J. Fluids Struct.* 76, 185–215.  
 Tezdogan, T., Incecik, A., Turan, O., 2015. A numerical investigation of the squat and resistance of ships advancing through a canal using CFD. *J. Mar. Sci. Technol.* 21 (1), 1–16.  
 Tezdogan, T., Demirel, Y.K., Kellett, P., Khorasanchi, M., Incecik, A., Turan, O., 2015. Full-scale unsteady RANS CFD simulations of ship behaviour and performance in head seas due to slow steaming. *J. Ocean Eng.* 97, 186–206.  
 Wei, Zhang, Zao-jian, Zou, De-heng, Deng, 2017. A study on prediction of ship maneuvering in regular waves. *J. Ocean Eng.* 137, 367–381.  
 Wei-min, Gong, You-zhan, Hu, 1982. A preliminary method for estimating ship resistance in shallow water. *Shipbuild. China* (3), 1–5.  
 Xin-le, Jia, Yan-sheng, Yang, 1999. Mathematical Model of Ship Motion. Dalian maritime university press.  
 Xiu-heng, Wu, 1998. Maneuverability and Seakeeping of Ships. Chian communication press.  
 Yasukawa, H., Yoshimura, Y., 2015. Introduction of MMG standard method for ship maneuvering predictions. *J. Mar. Sci. Technol.* 20 (1), 37–52.  
 Zou, Lu, Larsson, L., 2013. Numerical predictions of ship-to-ship interaction in shallow water. *J. Ocean Eng.* 72, 386–402.